Supporting Information for Publication

Suppression of dynamic disorder by electrostatic interactions in structurally close organic semiconductors

Andrey Yu. Sosorev[1,2*], Olga D. Parashchuk[2], Nikita V. Tukachev[1], Dmitry R. Maslennikov[1], Dmitry I. Dominskiy[2], Oleg V. Borshchev[3], Marina S. Polinskaya[3], Maxim S. Skorotetcky[3], Oleg G. Kharlanov[2], Dmitry Yu. Paraschuk[2*]

[1]Institute of Spectroscopy of the Russian Academy of Sciences, Fizicheskaya Str., 5, Troitsk, Moscow 108840, Russia

[2]Faculty of Physics, M.V. Lomonosov Moscow State University, Leninskie Gory 1/62, Moscow 119991, Russia

[3]Enikolopov Institute of Synthetic Polymeric Materials, Russian Academy of Science, Profsoyuznaya 70, Moscow 117393, Russia

*Corresponding authors: sosorev@physics.msu.ru, paras@physics.msu.ru

S1. Crystal structures: details

Crystal structures of BTBT (ccdc 975935), chrysene (ccdc 1131738), NDT (ccdc 812876), TTA (ccdc 1189330) and C8-BTBT (ccdc 679293) were previously reported in Refs. [1-5]; crystal structure of C8-TTA has not been resolved yet. Crystal structure parameters are given in Table S1. All crystals belong to monoclinic system and have layered structure: conjugated cores form herringbone layers via edge-to-face and edge-to-edge interactions (see Figure 4). In BTBT, chrysene and C$_8$-BTBT the layers lie in the *ab* plane, while in NDT they lie in *bc* plane and in TTA they correspond to (101) crystal plane. All crystals have inversion symmetry centers so that they have two types of vibrational modes: only IR-active and only Raman-active ones.

Table S1. Characteristics of the crystal structure for BTBT, chrysene, TTA and NDT.

Molecule	Z	Z_{red}	a, Å	b, Å	c, Å	α	β	γ	Space group
BTBT	2	2	8.1018(15)	5.8927(8)	11.9073(19)	90	106.443(6)	90	P 2$_1$/a
Chrysene	4	2	8.386	6.196	25.203	90	116.20	90	I 2/c
NDT	4	4	17.973(5)	7.4851(18)	8.244(2)	90	93.482(15)	90	P 2$_1$/c
TTA	2	2	11.462(1)	4.026(1)	10.437(1)	90	103.77(1)	90	P 2$_1$/n

S2. Raman spectra: details

Fig. S1 shows room-temperature Raman spectra of chrysene, NDT and TTA. Chrysene LF spectrum is in reasonable correspondence with the earlier data[6]; the other LF spectra are reported for the first time. From this figure it is clearly seen that LF Raman intensity is significantly

different in the crystals studied: it exceeds HF one in BTBT but is comparable to it for chrysene, TTA and NDT. Fig. S2 presents the corresponding spectra at 80K, as well as BTBT spectrum at the same temperature. Fig. S3 compares the LF Raman spectra of chrysene, BTBT, NDT, and TTA at room temperature and at 80 K. In brief, LF modes are shifted towards higher frequencies with cooling from room temperature to 80 K, which can be readily attributed to the thermal squeezing of the crystals. The LF Raman intensities decrease since the thermal population of the vibrational modes decreases. On the contrary, the HF Raman bands are slightly changed.
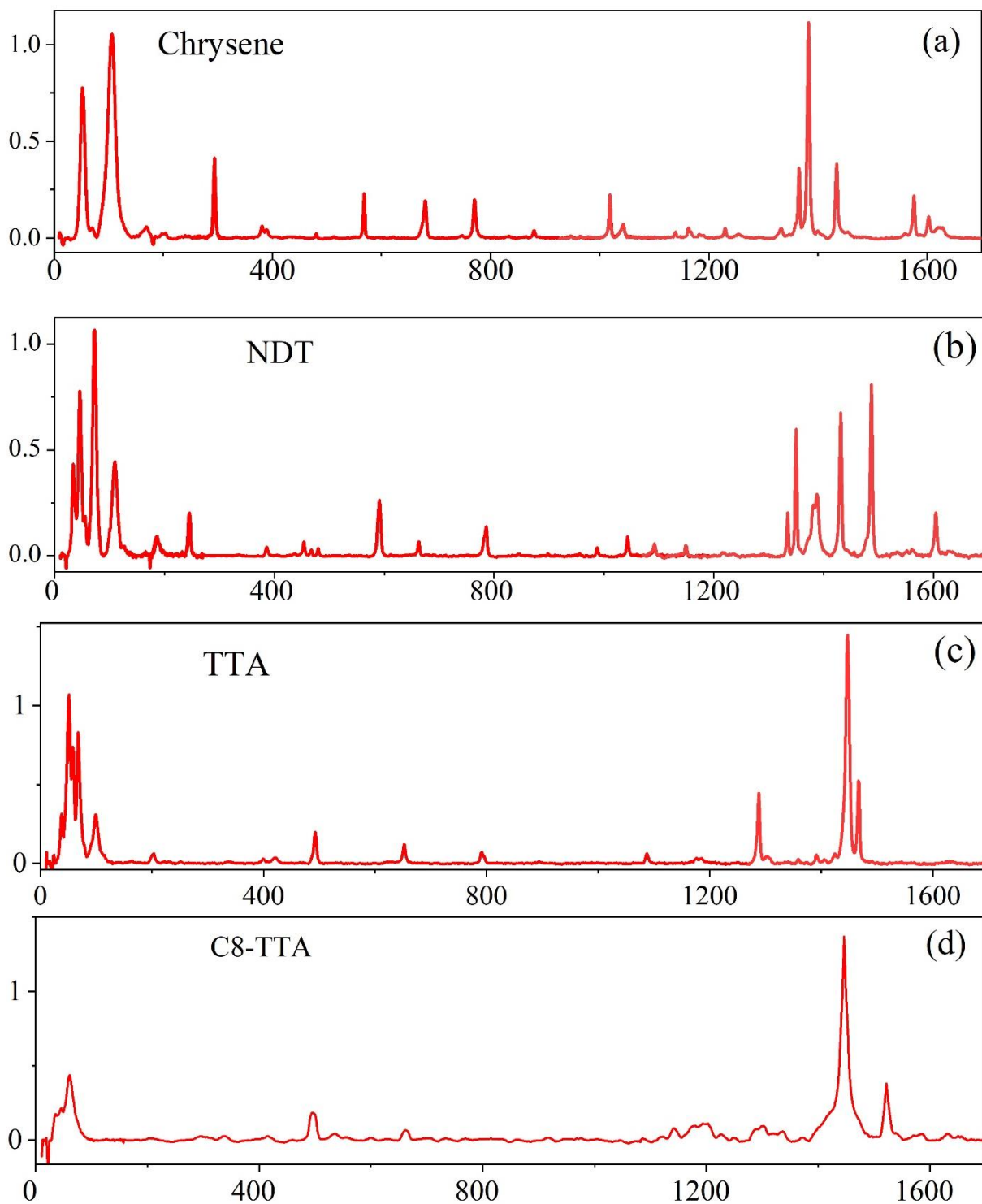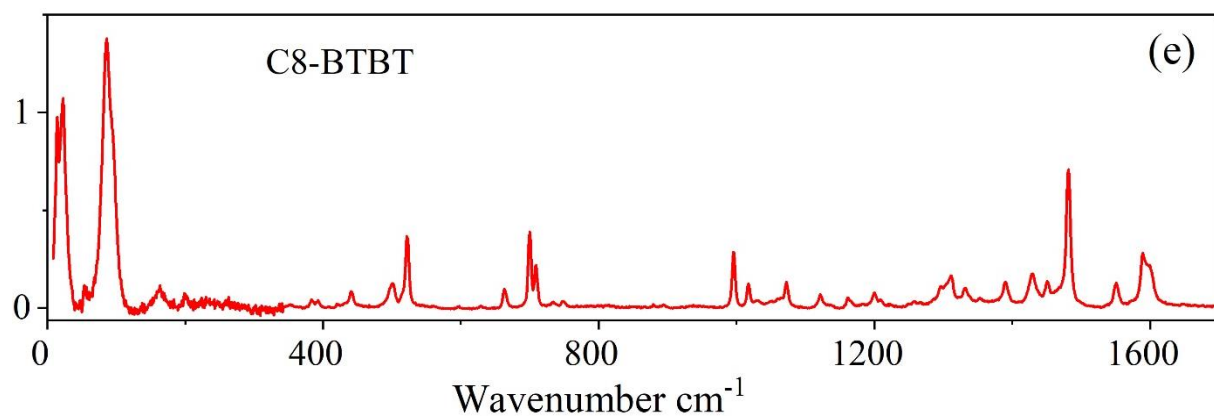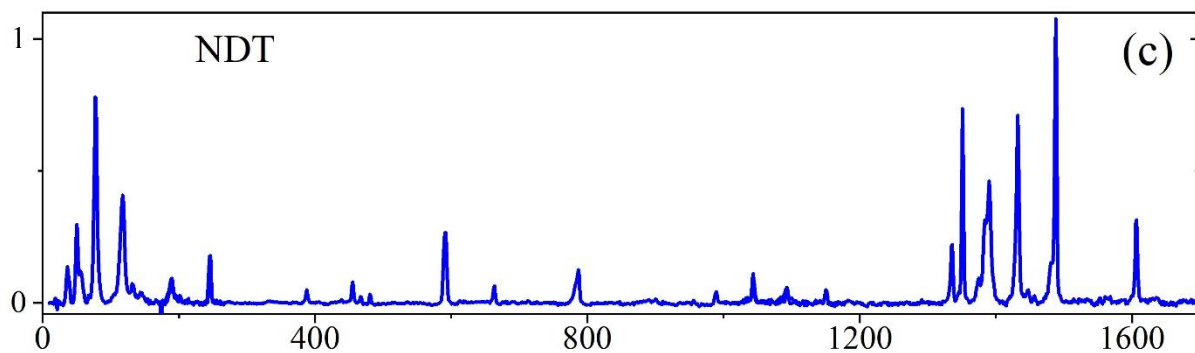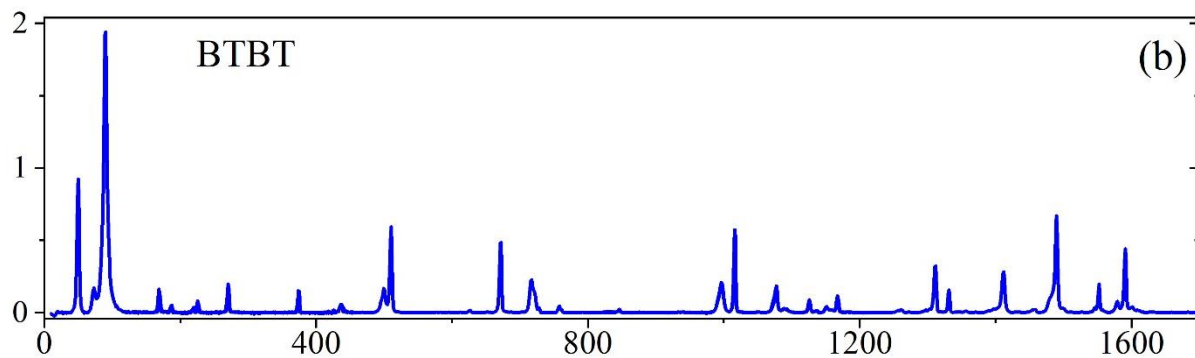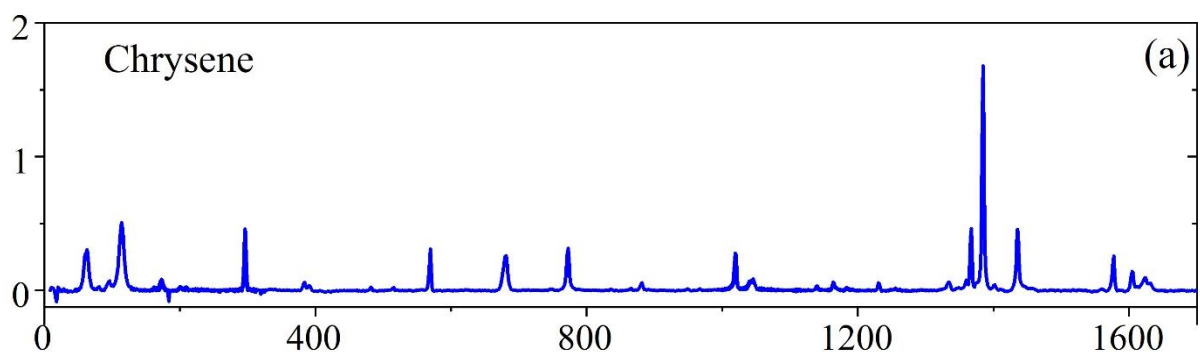
Fig. S1. Room-temperature Raman spectra for the compounds studied (chrysene, NDT, TTA, C_8-TTA and C_8-BTBT). The spectra were normalized to the integral over of the HF range (200–2000 cm^{-1}).
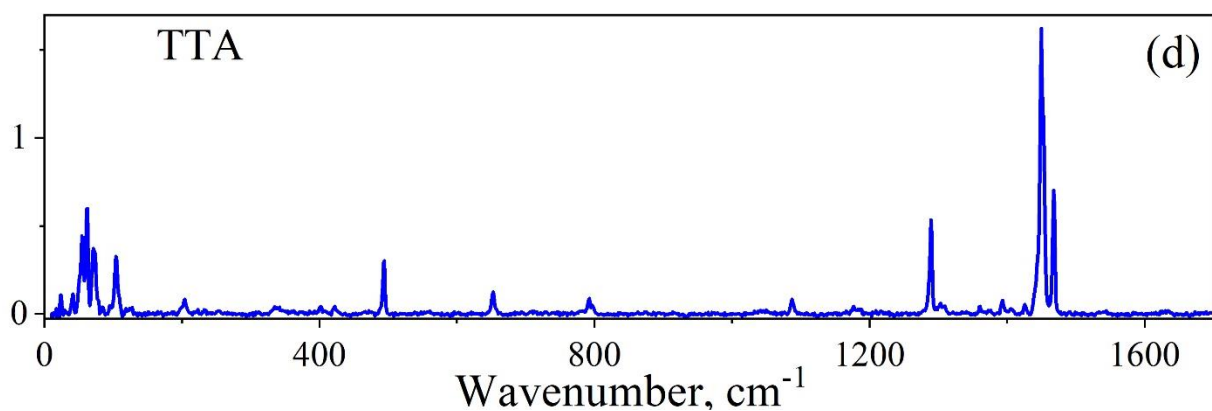
Fig. S2. Raman spectra of chrysene, BTBT, NDT and TTA at 80 K. The spectra were normalized to the integral over the HF range (200–2000 cm^{-1})
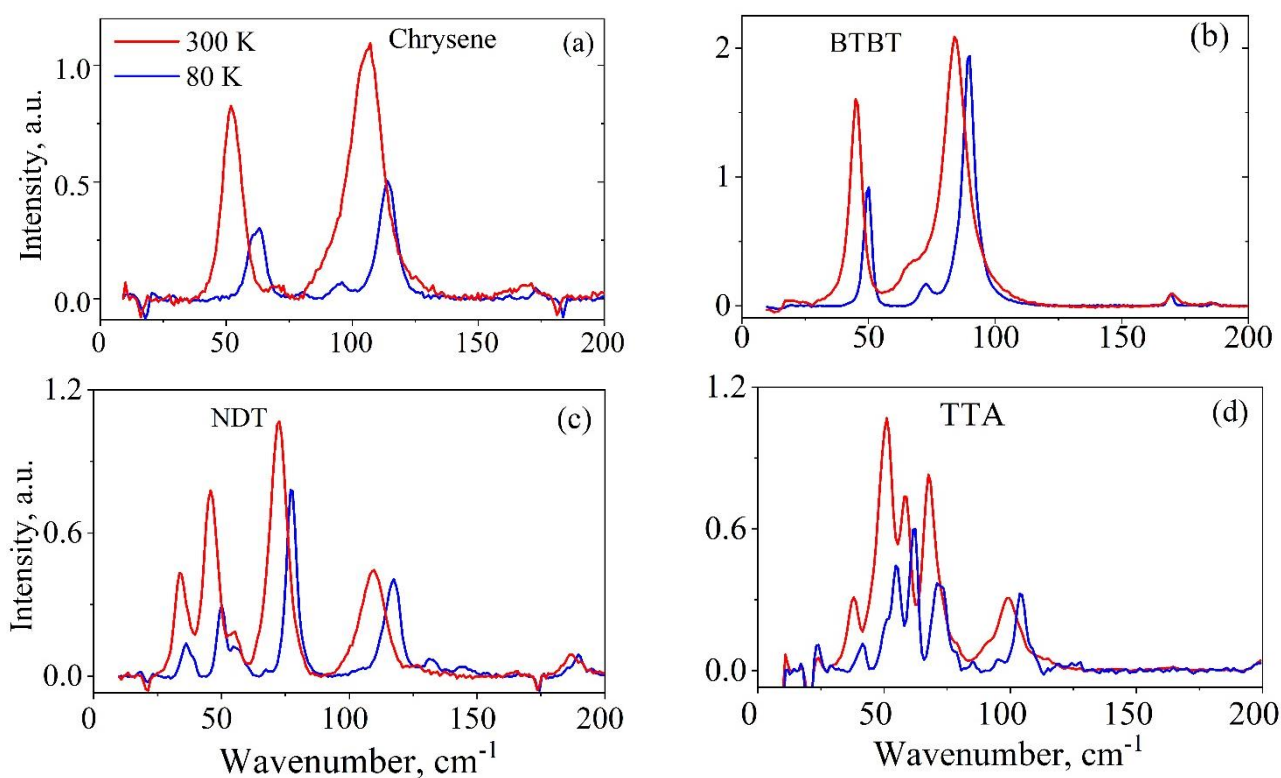

Fig. S3. LF Raman spectra of chrysene, BTBT, NDT and TTA at 300 K (red lines) and 80 K (blue lines). The spectra were normalized to the integral over the HF range (200–2000 cm^{-1}).

Comparison of C$_8$-BTBT and C$_8$-TTA spectra with those of unsubstituted compounds. Fig. S4 compares LF Raman spectra for C$_8$-BTBT and C$_8$-TTA with their unsubstituted counterparts. From this figure it follows that the LF spectrum of C$_8$-BTBT resembles that of BTBT and has two LF bands. The first band has lower frequency than that for BTBT (~23 cm^{-1} vs ~45 cm^{-1}), while the second one has the same frequency as for BTBT. As indicated in Section S3, the first band is associated with L_z, while the second is associated with L_x. The decrease of the first band's

4

frequency in C_8-BTBT as compared to BTBT can be readily explained by the increase of the molecular moment of inertia around the axis perpendicular to the molecular plane (z axis). On the contrary, the retained frequency of the second band can be explained by the nearly unaltered moment of inertia with respect to the long molecular (x) axis. This corroborates the results of the band assignment based on the solid-state DFT calculations for BTBT. For C_8-TTA, the shape of the spectrum is significantly different from that of TTA, which can be tentatively assigned to the different molecular packing in these crystals (note that crystal structure of C_8-TTA is unknown). Fig. S1d,e presents the Raman spectra of the two compounds in the range 10–1700 cm^{-1}.
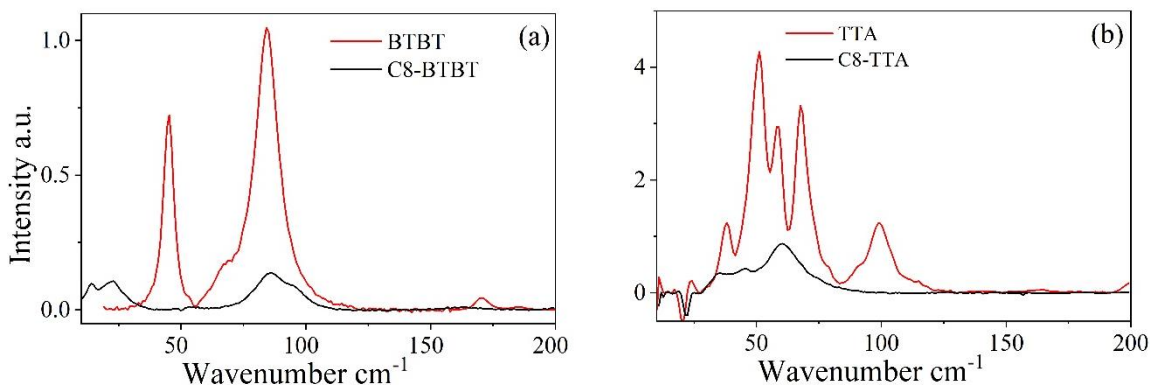

Fig. S4. LF Raman spectra of BTBT, C_8-BTBT (a) and TTA, C_8-TTA (b) at 300 K. The spectra were normalized to the integral Raman spectrum over the HF range (200–2000 cm^{-1}).

S3. Calculated Raman spectra

In the rigid-molecule approximation, the LF Raman-active vibrations of BTBT and chrysene correspond to six librations since $Z_{red} = 2$ in these crystals. The two lowest-frequency modes are molecular librations around the axis normal to the molecular plane; we will refer to these modes below as L_z. The two higher-frequency modes are librations around the short molecular axis (L_y), and the two highest-frequency LF Raman modes are librations around the long molecular axis (L_x). This is natural since the molecular moment of inertia decreases from the z to the y and the x axes. This simple reasoning is confirmed by solid-state DFT calculations (see Fig. S5a-d). Similarly, for TTA and NDT the modes with the strongest Raman intensity are librations (see Fig. S5e-h).

BTBT   chrysene

a) 47 cm^{-1} L_z c) 62 cm^{-1} L_z

b) 90 cm^{-1} L_x d) 121 cm^{-1} L_x

TTA   NDT

e) 68 cm^{-1} g) 69 cm^{-1}

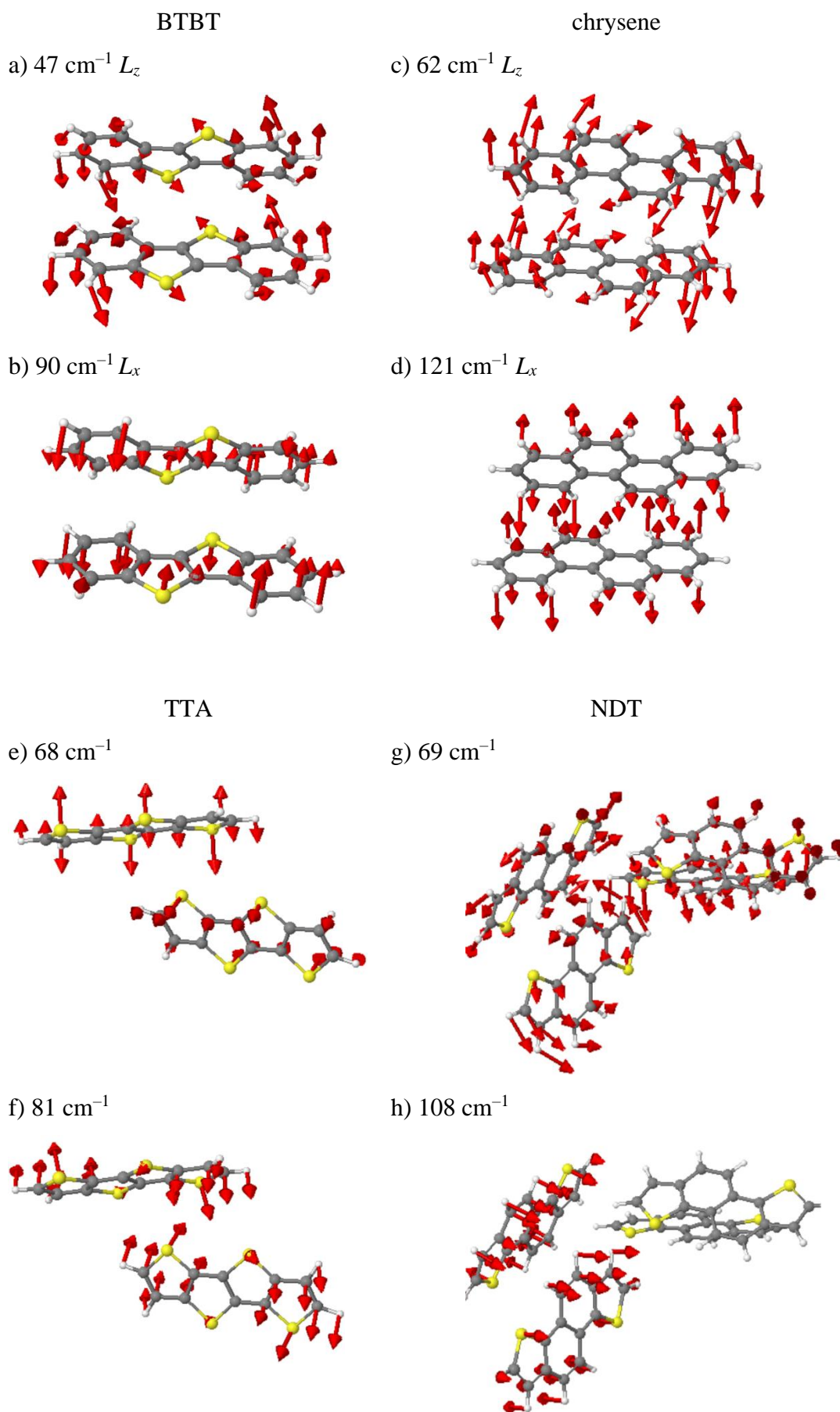f) 81 cm^{-1} h) 108 cm^{-1}

Fig. S5. Atomic displacements for the strongest Raman-active LF vibrational modes of BTBT (a,b), chrysene (c, d), TTA (e,f) and NDT (g,h).

6

S4. Transfer integrals and their vibrational modulation

Table S2. Average (equilibrium-state) $|J|$, its standard deviation σ_J, and ratio σ_J/J.

Compound	$|J|$, meV		σ_J, meV		Average σ_J/J	
	B3LYP	CAM-B3LYP	B3LYP	CAM-B3LYP	B3LYP	CAM-B3LYP
chrysene	35	39	8	9		
	41	45	9	10	0.13	0.14
	67	75	14	17		
	52	55	12	11		
BTBT	6	5	11	12	0.31	0.32
	1	2	8	11		

S5. Reorganization energies and optical bandgaps

Table S3 presents the calculated λ and E_g (at various levels of theory) and collates the latter with the experimental data (see spectra in Fig. S6). E_g were calculated using three popular functionals, namely, B3LYP, PBE and CAM-B3LYP and basis set 6-31G(d,p) basis set; the results are presented in Table S3. For CAM-B3LYP, E_g were ~0.5 eV larger than those for B3LYP, while for PBE, they were ~0.2-0.5 eV lower than for B3LYP; nevertheless, for all the three functionals, E_g for chrysene and NDT were ~1 eV larger than those for BTBT and TTA. From Table S3 it follows that B3LYP functional provides excellent agreement with the experiment, which is in line with previous studies.[7] A larger basis set 6-311G(d,p) yielded nearly identical to those obtained at 6-31G(d,p) level (using B3LYP as functional). Curiously, the difference in E_g is not the main factor determining the relative σ_J/J (estimated from the Raman data) in the OSs studied: even assuming identical E_g, the largest $(\sigma_J/J)_{Raman}$ is obtained for TTA, and the lowest – for chrysene (cf. Fig. S6b and Fig. 4a). On the contrary, assuming identical λ for the OSs studied, Eq. (3) predicts the largest $(\sigma_J/J)_{Raman}$ not for TTA but for BTBT, and the correlation between the dynamic disorder and reciprocal energy of the intermolecular interactions is deteriorated.

Table S3. Reorganization energies and optical bandgaps for the unsubstituted compounds studied.

	λ, meV	Calculated E_g, eV[a]				Experimental E_g, eV[b]
		B3LYP		CAM-B3LYP	PBE	
		6-31G(d,p)	6-311G(d,p)	6-31G(d,p)		
BTBT	220	3.9	3.9	4.4	3.5	3.9
chrysene	161	4.7	4.7	5.2	4.2	4.7
NDT	268	4.6	4.6	5.1	4.3	4.6
TTA	315	3.8	3.8	4.2	3.6	3.9

[a] Approximated in calculations as the energy of the lowest-energy transition with the oscillator strength exceeding 0.15. [b] Lowest-energy absorption peak with the intensity more than 0.2 of the absorption maximum, see Fig. S6.
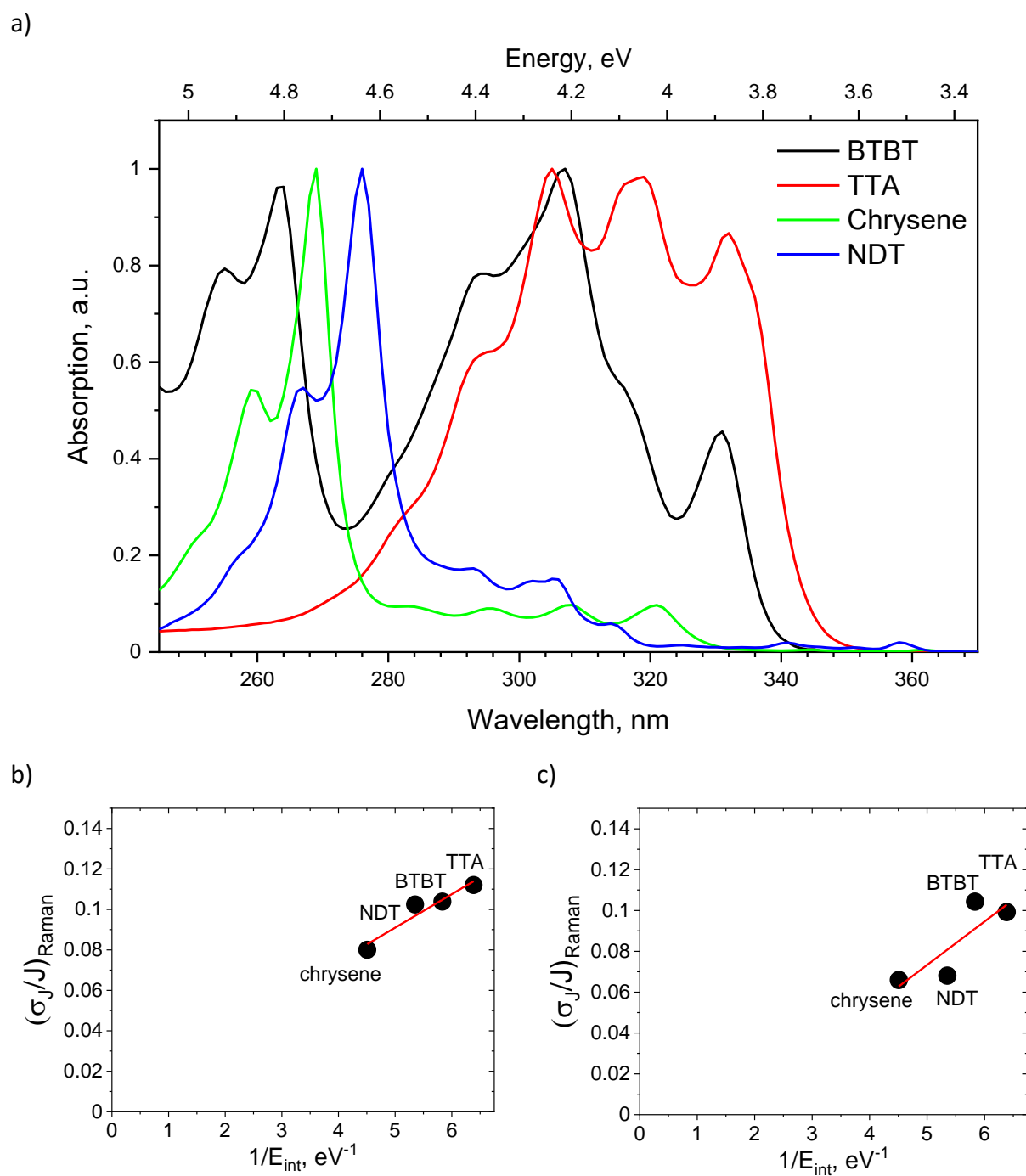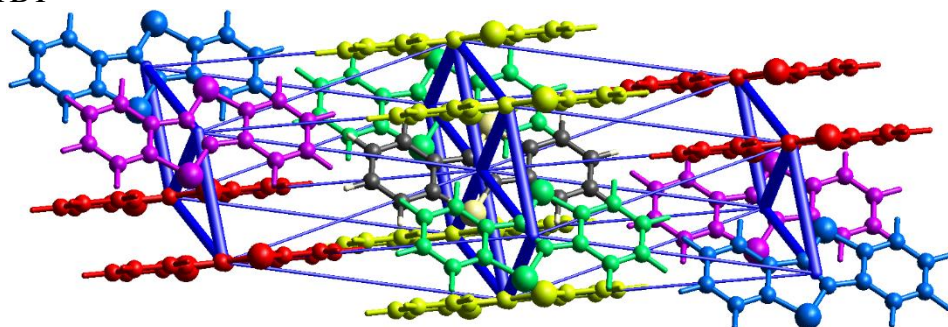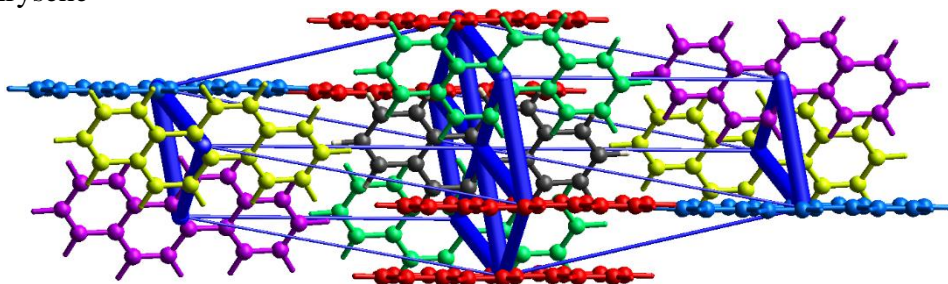
Fig. S6. a) Absorption spectra in diluted (~10^{-5} M^{-1}) THF solutions of the compounds studied. b,c) Correlation between the reciprocal total energy of intermolecular interactions $1/E_{int}$ and σ_J/J estimated from the Raman data (see Eq. (3)) assuming identical E_g=4 eV (b) or identical λ=0.2 eV (c); the red lines are linear fits.

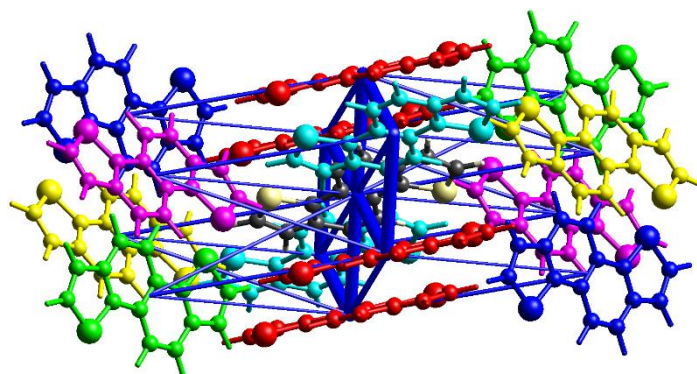## S6. Intermolecular interactions: details

a) BTBT
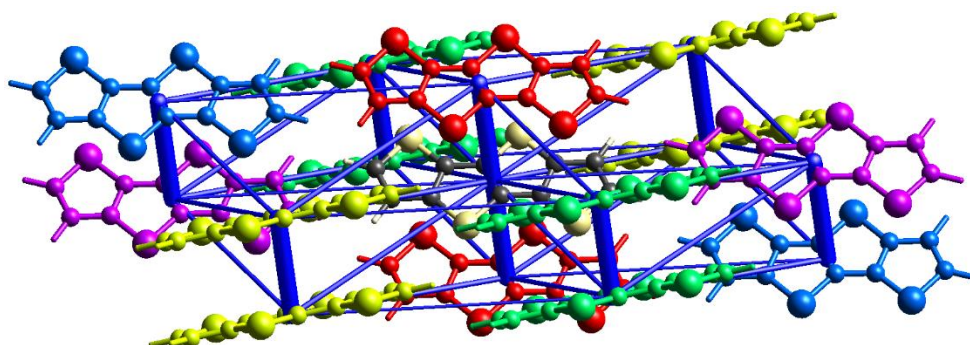

b) Chrysene

c) NDT

d) TTA

Fig. S7. Graphical representation of intermolecular interactions in BTBT, chrysene, NDT and TTA crystals. The cylinders link molecular centroids, and their thickness is proportional to the magnitude of the energy; for clarity, pairwise energies with magnitudes less than 5 kJ mol^{-1} are omitted. Equivalent pairs with center black molecule have the same color. For details see Table S4-S7.

Fig. S7 presents the patterns of the total intermolecular energy, i.e. the sum of electrostatic, dispersion, polarization and repulsion energies, for the four compounds studied. Table S9 sums up interaction energies between the central molecule (black) and molecules within the layer and

outside the layer. Note an ambiguity in using term 'layer' in the crystals of organic semiconductors (cf. e. g. Refs. 8 and 9; we use this term according to the former). As a result, the total energy of the intermolecular interactions is the lowest for BTBT and TTA, which enables strong dynamic disorder. On the contrary, stronger inter- or intralayer interactions in chrysene and NDT presumably result in the suppressed LF vibrations in these crystals.

Table S4. Different interaction energies of the molecular pairs for BTBT in kJ mol^{-1}. N is the number of pairs, R is the distance between the molecule centroids, E_ele is the classical electrostatic energy of interaction between monomer charge distributions, E_pol is the polarization energy estimated as a sum over atoms with terms of the kind $-\frac{1}{2}\alpha|\boldsymbol{F}|^2$, where the electric field $\boldsymbol{F}$ is computed at each atomic nucleus from the charge distribution of the other monomer and α are isotropic atomic polarizabilities, E_dis is Grimme's D2 dispersion correction summed over all intermolecular atom pairs, E_rep is the exchange–repulsion energy, obtained from the antisymmetric product of the monomer spin orbitals,[10] and E_tot is the total energy.

	N	R (A)	E_ele	E_pol	E_dis	E_rep	E_tot
🔴	4	11.81	–0.8	–0.3	–8.3	4.7	–5.4
🟡	4	5.01	–9.2	–1.3	-38.4	31.5	–24.6
🟢	2	5.89	–10.0	–1.0	–26.3	25.2	–18.6
🔵	2	13.29	0.5	–0.1	–1.3	0.1	–0.5
🟣	2	11.91	–1.8	–0.3	–8.5	4.8	–6.6

Table S5. Different interaction energies of the molecular pairs for chrysene in kJ mol^{-1}.

	N	R (A)	E_ele	E_pol	E_dis	E_rep	E_tot
🔴	4	5.21	–9.4	–1.9	–47.1	28.9	–34.5
🟡	2	11.80	–2.3	–0.3	–9.6	5.6	–7.5
🟢	2	6.20	–7.3	–1.1	–27.5	12.7	–24.6
🔵	2	12.60	–1.5	–0.1	–6.9	3.5	–5.5
🟣	2	11.80	0.1	–0.3	–9.3	6.3	–4.3

Table S6. Different interaction energies of the molecular pairs for NDT in kJ mol^{-1}.

	N	R (A)	E_ele	E_pol	E_dis	E_rep	E_tot
🔴	4	5.57	–6.3	–1.2	–37.7	22.1	–26.7
🟡	2	9.66	–3.6	–0.6	–10.9	7.9	–8.9
🟢	2	9.73	–4.1	–0.5	–10.8	10.2	–7.8
🔷	2	8.24	–4.4	–0.5	–16.3	9.4	–13.4
🔵	2	9.73	–0.2	–0.4	–8.4	6.4	–3.9
🟣	2	10.11	–2.1	–0.3	–7.1	4.3	–6.0

Table S7. Different interaction energies of the molecular pairs for TTA in kJ mol^{-1}.

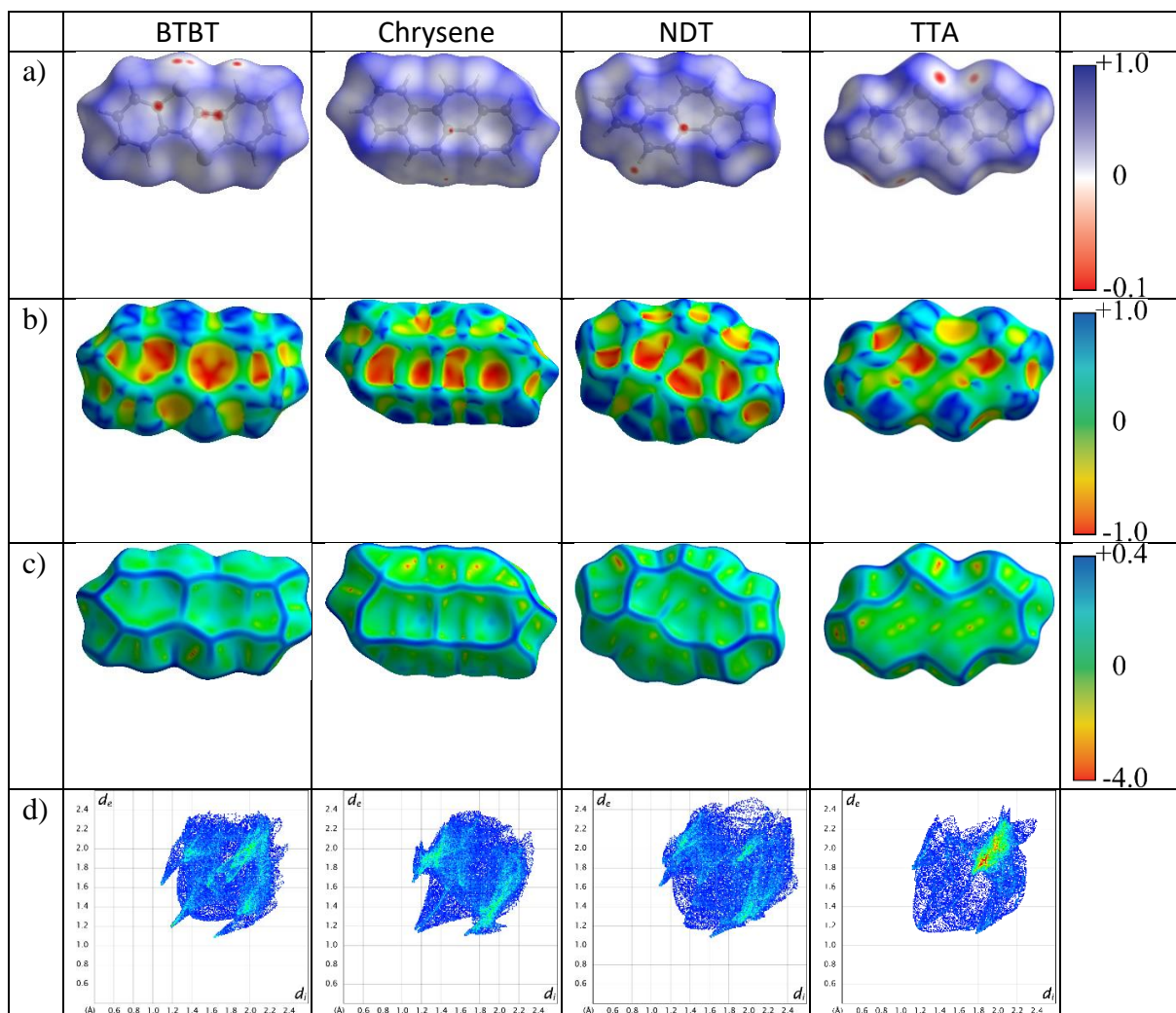|	N	R (A)	E_ele	E_pol	E_dis	E_rep	E_tot
🟥	2	4.03	–9.5	–1.7	–55.8	45.9	–31.6
🟨	4	8.85	–5	–0.8	–13.8	12	–10.6
🟩	4	7.06	–12.1	–0.4	–18.1	32.6	–8.7
🟦	2	12.15	0.2	–0.5	–4.4	2.7	–2.4
🟪	2	11.46	–2.8	–0.7	–9.3	9.4	–5.7

Fig. S8. Hirshfeld surfaces of BTBT, chrysene, NDT and TTA mapped with (a) normalized contact distance, (b) shape index S and (c) curvedness C. The Hirshfeld surface defines the space occupied by a molecule: inside this surface, the electron density from the given molecule is larger than that from the others. Red spots in (a) indicate intermolecular contacts closer than the sum of the van der Waals radii (close contacts), blue spots are referred to longer contacts, and contacts around the sum of van der Waals radii (moderate contacts) are white. (d) 2D finger print plots with d_i and d_e ranging from 0.5 to 2.9 Å. For any given d_i and d_e pairs, the change in color shows the raise in occurrence: white color for no occurrence, then blue green and red for most frequent occurrence.
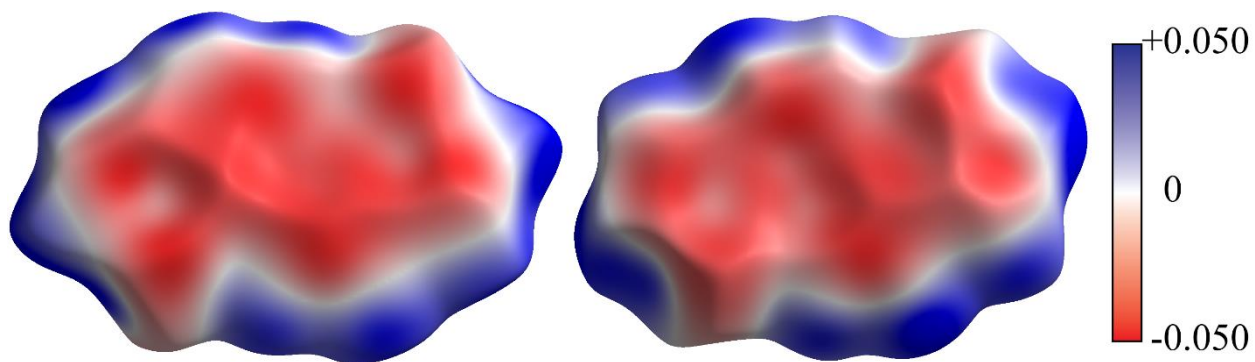
Fig. S9. ESP mapping of the Hirshfeld surfaces for the two nonequivalent molecules of NDT.

For chrysene, ESP is negative at the molecular faces and positive at the molecular edges; Noteworthily, in NDT C···H (and S···H) close contacts between the layers have the smallest distance as compared to BTBT and chrysene (2.96A vs 3.07A and 3.11A respectively, see Fig. S10). On the contrary, for BTBT, these areas are deep inside the layer (Fig. 4d) and cannot interact with the adjacent layers — this explains the similar interlayer interaction energies for BTBT and chrysene (Fig. 4b).
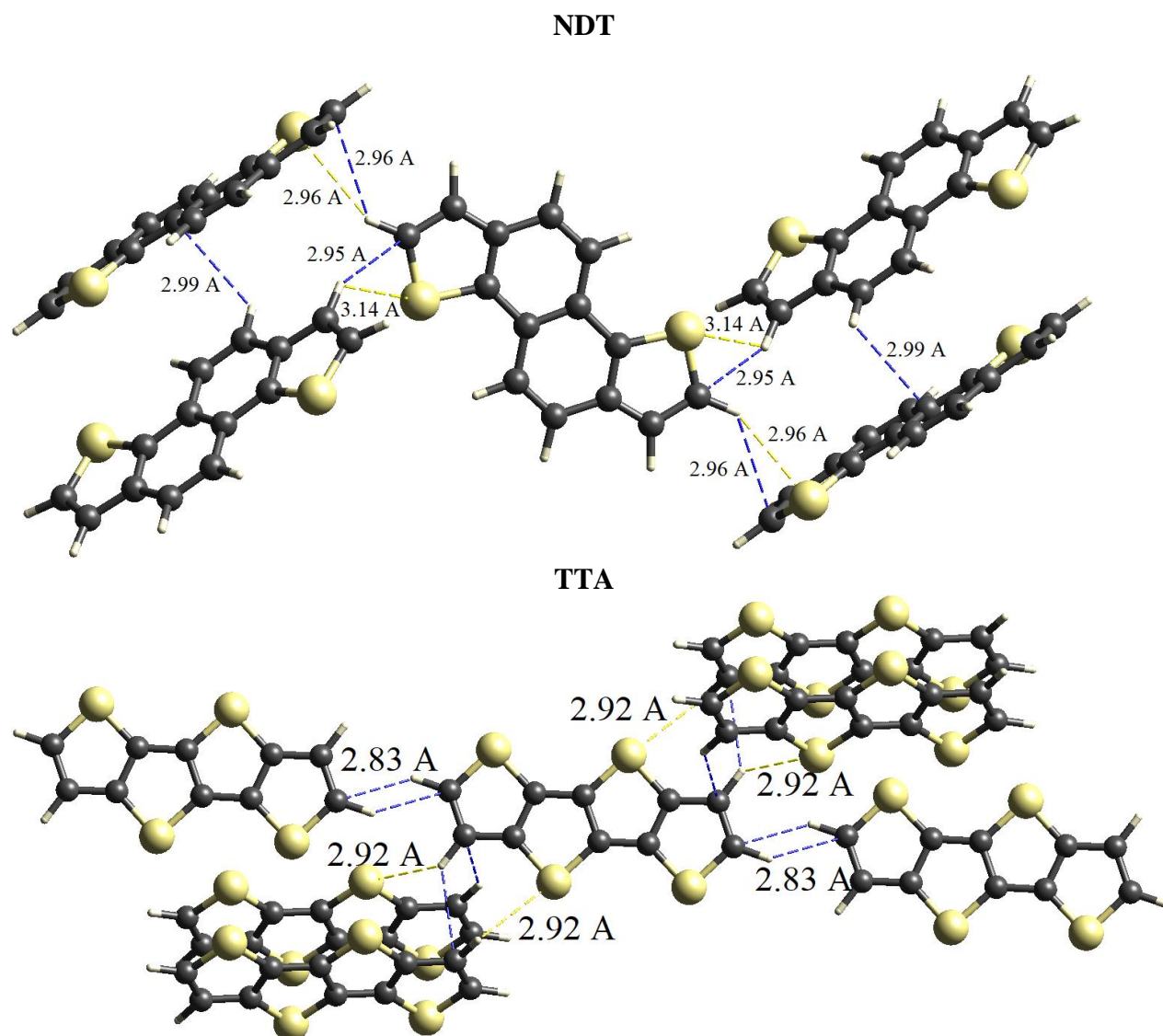
NDT

TTA
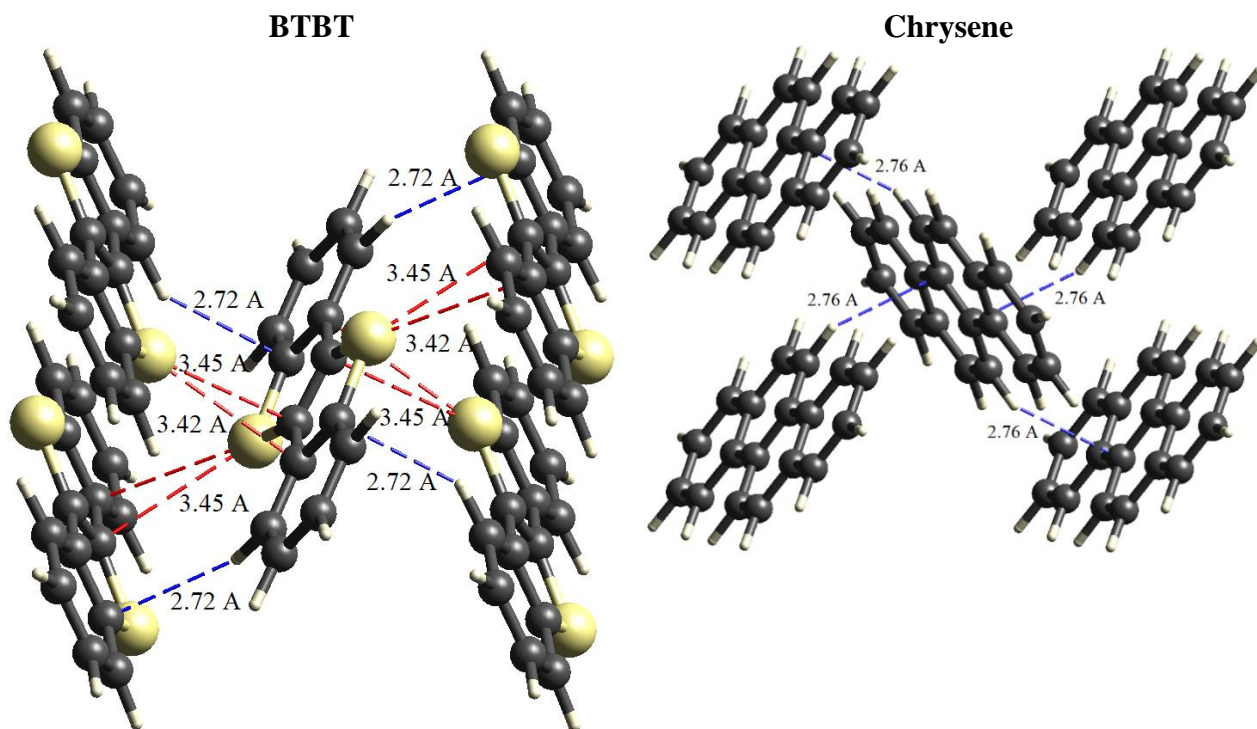
Fig. S10. Close contacts for BTBT (a), chrysene (b), NDT (c) and TTA (d) as obtained from Hirshfeld analysis. Blue for C···H contacts, yellow for S···H contacts and red for S···C contacts.
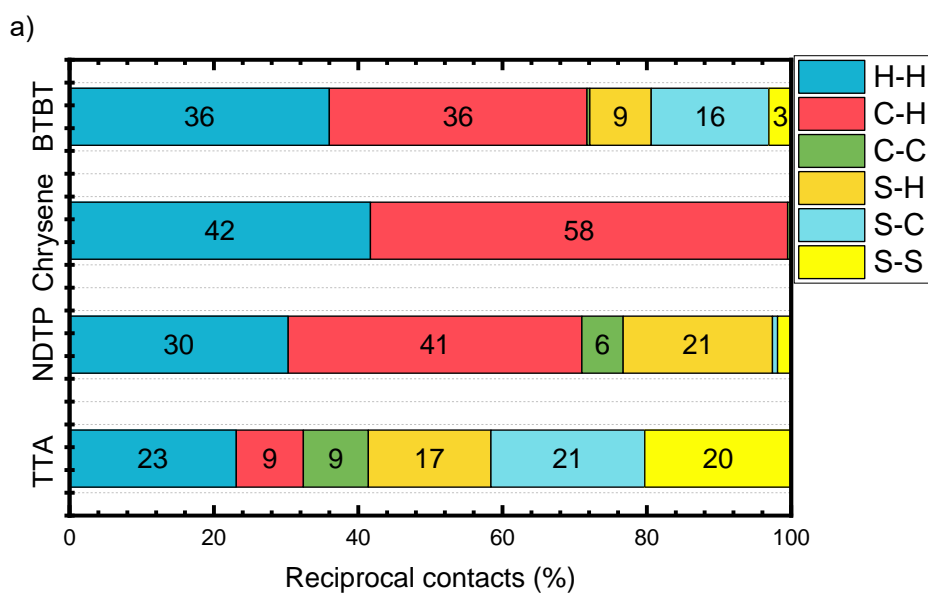
a)

Fig. S11. Distribution of reciprocal intermolecular contacts for BTBT, chrysene, NDT and TTA arranged by molecules.
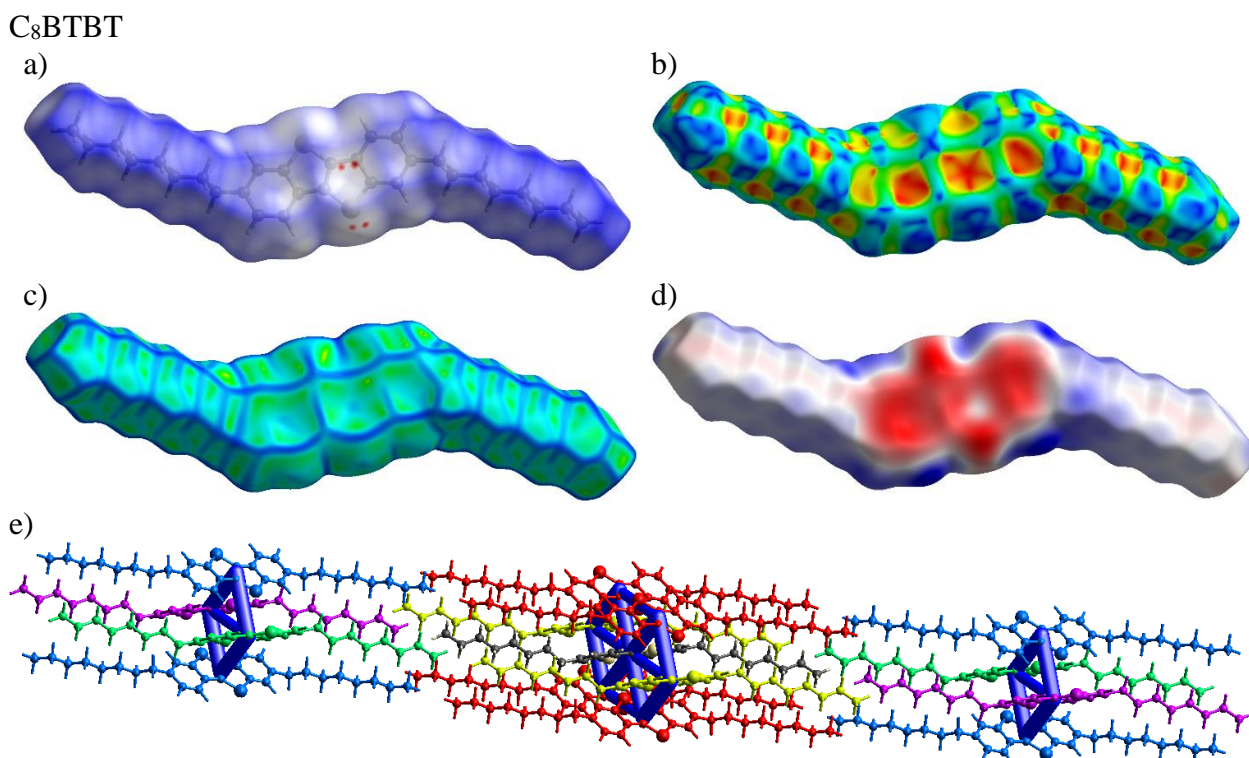
C$_8$BTBT

Fig. S12. Hirshfeld surface of C8-BTBT mapped with (a) normalized contact distance, (b) shape index S, (c) curvedness C and (d) ESP. Red spots in (a) indicate intermolecular contacts closer than the sum of the van der Waals radii (close contacts), blue spots are referred to longer contacts, and contacts around the sum of van der Waals radii (moderate contacts) are white. (e) Graphical representation of intermolecular interactions in C8-BTBT crystal. The cylinders link molecular centroids, and their thickness is proportional to the magnitude of the energy; for clarity, pairwise energies with magnitudes less than 5 kJ mol^{-1} are omitted. The scaling is the same as in Figures S8-9.

Table S8. Different interaction energies of the molecular pairs for C$_8$-BTBT in kJ mol^{-1}.

	N	R	E_ele	E_pol	E_dis	E_rep	E_tot
🟥	4	4.93	−12.2	−2.0	−88.0	51.1	−59.5
🟨	2	5.93	−13.5	−1.6	−62.7	46.7	−41.2
🟩	2	30.02	−1.0	−0.0	−8.0	5.2	−4.8
🟦	4	31.12	−0.1	−0.0	−2.0	0.2	−1.6
🟪	2	31.96	−0.5	−0.0	−3.9	2.2	−2.6

Table S9. Total interaction energies within and between the layers.

	interlayer					intralayer				
BTBT	Chrysene	NDT	C$_8$-BTBT	TTA	BTBT	Chrysene	NDT	C$_8$-BTBT	TTA
−35.8	−34.6	−53.2	−21.2	−58.6	−135.6	−187.2	−133.6	−320.4	−98

S7. Experimental details

The Raman microscope (inVia, Renishaw) with a 50× objective lens (Leica DM 2500 M, NA = 0.5) and equipped by He–Ne laser (RL633, Renishaw) was used for Raman measurements. In the LF range (10–200 cm^{-1}) the measurements were made with a built-in double monochromator with subtraction of dispersion in the confocal regime (NExT monochromator, Renishaw). In the HF range (200–2000 cm^{-1}) the measurements were made with an edge-filter. A thermocell (Linkam) allows operation in the temperature range from 80 to 573 K. The cell was placed directly under the microscope. An objective with a numerical aperture of 0.5 and a working distance of 6 mm was used, which made it possible to study the sample directly inside the thermocell.

The background from the Raman spectra was subtracted by the cubic spline interpolation method. All the spectra were divided by the number of accumulations and acquisition time. The dips in the spectra at approximately 20 and 175 cm^{-1} are the artefacts of the measurements associated with the presence of dust particles on the NExT monochromator mirrors.

The acquisition time and number of accumulations were adjusted to maximize the signal-to-noise ratio with the minimal sample degradation. All the spectra for the powder samples were measured at several points and then averaged to reduce the anisotropy effect on the Raman spectra and to increase the single-to-noise ratio.

S8. Computational details

We used 1000 eV cutoff for initial unit cell relaxation and then 600 eV cutoff for fixed volume relaxation and single point calculations. All geometry optimizations were performed with tight criteria predefined in VASP. Γ-centered Monkhorst-Pack grid with k-spacing not exceeding 0.2 Å^{-1} and Gaussian smearing was used during geometry relaxation and phonon calculations. Linear response vibrational analysis was made using the dfpt procedure. Raman activities were estimated by means of numerical differentiation of macroscopic dielectric tensor along corresponding normal modes.

References

1.	Vyas, V. S.; Gutzler, R.; Nuss, J.; Kern, K.; Lotsch, B. V. Optical gap in herringbone and π-stacked crystals of [1]benzothieno[3,2-b]benzothiophene and its brominated derivative. *CrystEngComm* **2014,** *16* (32), 7389-7392.

2.	Burns, D. M.; Iball, J.; Robertson, J. M. Refinement of the structure of chrysene. *Proceedings of the Royal Society of London. Series A. Mathematical and Physical Sciences* **1960,** *257* (1291), 491-514.

3.	Shinamura, S.; Miyazaki, E.; Takimiya, K. Synthesis, properties, crystal structures, and semiconductor characteristics of naphtho[1,2-b:5,6-b']dithiophene and -diselenophene derivatives. *J Org Chem* **2010,** *75* (4), 1228-34.

4.	Mazaki, Y.; Kobayashi, K. Crystal and molecular structure of thieno[2″,3″:4′,5′]thieno[2′,3′-d]thieno-[3,2-b]thiophene as a hydrogen-poor heterocycle. *Journal of the Chemical Society, Perkin Transactions 2* **1992,** (5), 761-764.

5.	Izawa, T.; Miyazaki, E.; Takimiya, K. Molecular Ordering of High-Performance Soluble Molecular Semiconductors and Re-evaluation of Their Field-Effect Transistor Characteristics. *Advanced Materials* **2008,** *20* (18), 3388-3392.

6.	Capitani, F.; Höppner, M.; Malavasi, L.; Marini, C.; Dore, P.; Boeri, L.; Postorino, P. The effect of high pressure on the lattice structure and dynamics of phenacenes. *Journal of Physics: Conference Series* **2017,** *950*.

7. Ali, A.; Rafiq, M. I.; Zhang, Z.; Cao, J.; Geng, R.; Zhou, B.; Tang, W. TD-DFT benchmark for UV-visible spectra of fused-ring electron acceptors using global and range-separated hybrids. *Phys. Chem. Chem. Phys.,* **2020**, *22*, 7864–7874

8.	Cao, M.; Zhang, C.; Cai, Z.; Xiao, C.; Chen, X.; Yi, K.; Yang, Y.; Lu, Y.; Wei, D. Enhanced photoelectrical response of thermodynamically epitaxial organic crystals at the two-dimensional limit. *Nat Commun* **2019,** *10* (1), 756.

9.	Reddy, C. M.; Rama Krishna, G.; Ghosh, S. Mechanical properties of molecular crystals—applications to crystal engineering. *CrystEngComm* **2010,** *12* (8).

10.	Mackenzie, C. F.; Spackman, P. R.; Jayatilaka, D.; Spackman, M. A. CrystalExplorer model energies and energy frameworks: extension to metal coordination compounds, organic salts, solvates and open-shell systems. *IUCrJ* **2017,** *4* (Pt 5), 575-587.